
Magnetohydrodynamic Simulation Code

CANS+: Assessments and Applications

Yosuke MATSUMOTO^{1,2}, Yuta ASAHINA³, Yuki KUDOH¹, Tomohisa KAWASHIMA^{3,4}, Jin MATSUMOTO⁵, Hiroyuki R. TAKAHASHI³, Takashi MINOSHIMA⁶, Seiji ZENITANI⁴, Takahiro MIYOSHI⁷, and Ryoji MATSUMOTO¹

¹Department of Physics, Chiba University, 1-33 Inage-ku, Chiba, Chiba 263-8522

²Institute for Global Prominent Research, Chiba University, 1-33 Yayoi-cho, Inage-ku, Chiba 263-8522

³Center for Computational Astrophysics, National Astronomical Observatory of Japan, 2-21-1 Osawa, Mitaka, Tokyo 181-8588

⁴Division of Theoretical Astronomy, National Astronomical Observatory of Japan, 2-21-1 Osawa, Mitaka, Tokyo 181-8588

⁵Astrophysical Big Bang Laboratory, RIKEN, 2-1 Hirosawa, Wako, Saitama 351-0198

⁶Department of Mathematical Science and Advanced Technology, Japan Agency for Marine-Earth Science and Technology, 3173-25 Syowa-machi, Kanazawaku, Yokohama, 236-0001

⁷Department of Physics, Hiroshima University, 1-3-1 Kagamiyama, Higashi Hiroshima, Hiroshima 739-8526

*E-mail: ymatumot@chiba-u.jp

Received ; Accepted

Abstract

We present a new magnetohydrodynamic (MHD) simulation code with the aim of providing accurate numerical solutions to astrophysical phenomena where discontinuities, shock waves, and turbulence are inherently important. The code implements the HLLD approximate Riemann solver, the fifth-order-monotonicity-preserving interpolation scheme, and the hyperbolic divergence cleaning method for a magnetic field. This choice of schemes significantly improved numerical accuracy and stability, and saved computational costs in multidimensional

problems. Numerical tests of one- and two-dimensional problems showed the advantages of using the high-order scheme by comparing with results from a standard second-order TVD scheme. The present code enabled us to explore long-term evolution of a three-dimensional global accretion disk, in which compressible MHD turbulence saturated at much higher levels via the magneto-rotational instability than that given by the second-order scheme owing to the adoption of the high-resolution, numerically robust algorithms.

Key words: Magnetohydrodynamics (MHD) — Methods: numerical — Shock waves — Turbulence

1 Introduction

In the last decades, computational astrophysics has emerged together with the rapid growth of computational capabilities, enabling us to reveal various aspects of astrophysical phenomena that cannot be provided by observations. Among them, magnetohydrodynamic (MHD) simulations are powerful tools for understanding space and astrophysical phenomena such as solar flares and coronal mass ejections, auroral substorms in the terrestrial magnetosphere, magnetic dynamos in accretion disks and associated jet accelerations. In most cases, the systems are dominated by various MHD discontinuities, shock waves, and turbulence in which the fluid dynamics are strongly coupled with the magnetic field. Such highly nonlinear systems have stimulated the search for numerical algorithms that can solve the MHD equations with both high accuracy and stability.

Early development of MHD simulation codes was based on finite difference schemes with artificial and/or numerical dissipation, such as the modified Lax–Wendroff scheme (Rubin and Burstein 1967; Shibata 1983). The high-order upwind scheme was implemented in the ZEUS code (Stone et al. 1992; Hawley and Stone 1995) and has been used for many applications in astrophysics owing to its simplicity and flexibility. However, besides these early successes in computational astrophysics, overcoming spurious (grid) oscillations in highly stratified, compressible MHD applications has remained a task for further improvement in the numerical schemes (e.g., Kudoh et al. 1999).

Modern MHD simulation codes have a strategy of accurately capturing shock waves as the latter are usually accompanied by supersonic flows in space and astrophysical phenomena. Such shock-capturing schemes are based on the finite volume method in which the time evolution of cell-averaged conservative variables of the MHD equations is calculated from numerical fluxes at the cell surfaces. Thus, the accuracy and the robustness rely on the method of obtaining the numerical flux from the cell-averaged conservative variables.

In the numerical flux calculation, upwind natures are incorporated by solving a Riemann problem at the cell interface initiated with the two neighboring cell states. The so-called Godunov schemes are based on the idea that the numerical flux can be obtained by integrating the conservative variables in the Riemann fan following the conservation laws in space and time. For numerical solutions to the Riemann problem, various approximate Riemann solvers have been developed including the Roe's scheme (Roe 1981) and a family of HLL solvers (Harten et al. 1983; Li 2005; Miyoshi and Kusano 2005). Among them, the HLLD approximate Riemann solver of Miyoshi and Kusano (2005) is now the standard method in modern MHD codes (see e.g., Kritsuk et al. 2011) as it provides tractable and stable numerical solutions.

Special care must be taken in multidimensional MHD simulations as the solenoidal property of the magnetic field cannot be straightforwardly satisfied, and numerical errors from the divergence-free condition severely affect results, in particular, when solving the conservative forms of the MHD equations numerically. While divergence cleaning methods aim at maintaining the numerical errors within minimal levels by making modifications to the base equations (Brackbill and Barnes 1980; Powell et al. 1999; Dedner et al. 2002), the constrained-transport (CT) algorithm (Evans and Hawley 1988) accomplishes the divergence-free condition within a level of machine round-off errors by adopting a special discretization for the magnetic field. Nowadays, most MHD codes employ variants of the CT algorithm while preserving the upwind nature for the induction equation of the magnetic field (Londrillo and Del Zanna 2004; Gardiner and Stone 2005; Lee and Deane 2009; Miyoshi and Kusano 2011; Minoshima et al. 2015). For further information, readers may consult comprehensive comparisons of the schemes by Toth (2000), and also by Miyoshi and Kusano (2011) with more recent schemes.

Extensions of the scheme to a higher-order accuracy have been accomplished by adopting piecewise high-order polynomials to reconstruct variables' profiles in each cell used for the local Riemann problem at the cell interface, with which the total variation diminishing (TVD) property has been necessarily incorporated by adopting various slope limiters, so that the profiles degrade to the first order around discontinuities. The so-called MUSCL scheme (van Leer 1979) and its extension of the third-order PPM scheme (Colella and Woodward 1984) have been widely implemented for practical uses in public MHD codes as FLASH (Lee and Deane 2009; Lee 2013), PLUTO (Mignone et al. 2007), and Athena (Stone et al. 2008). See also Kritsuk et al. (2011) for other MHD codes. Note, however, that the overall spacial accuracy of these CT-based MHD codes has been achieved only up to the second order because the original CT algorithm is based on the second-order discretization. Third-order scheme has been proposed in the framework of the upwind CT (UCT) with additional large computational costs arising from high-order reconstructions and solutions of the Riemann problem at

the cell edge (Londrillo and Del Zanna 2004). A simple and cost-effective, fifth-order scheme was proposed by adopting the hyperbolic divergence cleaning method (Dedner et al. 2002) by Mignone et al. (2010). We have adopted a similar strategy as described in the present paper.

The Coordinated Astronomical Numerical Software, CANS, was developed for the Japanese astrophysical community by T. Yokoyama at the University of Tokyo and collaborators, and is publicly available with documents at the website <http://www-space.eps.s.u-tokyo.ac.jp/~yokoyama/etc/cans/>. The base schemes are the modified Lax–Wendroff scheme and the CIP–MOCCT scheme (Yabe et al. 2001; Kudoh et al. 1999), but the Roe–MUSCL scheme is also available. Additional physics modules of heat conduction and radiative cooling, and many application modules are also included. A physical problem can be easily solved by choosing the numerical schemes and visualizing by prebuilt Interactive Data Language (IDL) procedures, from which researchers and graduate students benefit when starting their simulation studies. CANS has been used in space and astrophysical applications since its start in 2002 (e.g., Asai et al. 2004; Isobe et al. 2005; Hanayama et al. 2005; Tao et al. 2005; Tsubouchi 2009; Toriumi and Yokoyama 2011).

CANS+ (CANS-plus) was designed based on the CANS philosophy, but has implemented the state-of-the-art numerical algorithms and parallelization. The codes are written in Fortran90/95 and are organized in a modular way as in CANS. Hybrid parallelization is implemented by using the MPI library and OpenMP for effective parallel scaling on modern massive parallel supercomputer systems. The code can be downloaded from the CANS+ documentation website <http://www.astro.phys.s.chiba-u.ac.jp/cans/doc/>. In this paper, we detail the numerical algorithms adopted in CANS+ in Section 2 and show assessments of the code’s capability with various physical problems in Section 3. As an application of CANS+, we present three-dimensional (3D) global simulations of a black hole accretion disk and discuss how the selection of the numerical schemes affects the angular momentum transport and the resulting mass accretion rate during its long-term evolution in Section 4. A summary of the paper and future perspectives are given in Section 5.

2 CANS+

2.1 Basic equations

CANS+ solves normalized MHD equations in semiconservative forms as

$$\frac{\partial \rho}{\partial t} + \nabla \cdot (\rho \mathbf{v}) = 0, \quad (1)$$

$$\frac{\partial \rho \mathbf{v}}{\partial t} + \nabla \cdot (\rho \mathbf{v} \mathbf{v} + p_t \mathbf{I} - \mathbf{B} \mathbf{B}) = \rho \mathbf{g}, \quad (2)$$

$$\frac{\partial \mathbf{B}}{\partial t} + \nabla \cdot (\mathbf{v} \mathbf{B} - \mathbf{B} \mathbf{v} + \psi \mathbf{I}) = -\nabla \times (\eta \mathbf{j}), \quad (3)$$

$$\frac{\partial e}{\partial t} + \nabla \cdot ((e + p_t) \mathbf{v} - \mathbf{B}(\mathbf{v} \cdot \mathbf{B})) = -\nabla \cdot (\eta \mathbf{j} \times \mathbf{B}) + \rho \mathbf{v} \cdot \mathbf{g}, \quad (4)$$

$$\frac{\partial \psi}{\partial t} + c_h^2 \nabla \cdot \mathbf{B} = -\frac{c_h^2}{c_p^2} \psi, \quad (5)$$

where ρ , \mathbf{v} , \mathbf{g} , \mathbf{B} , and e are the mass density, the velocity, the gravitational acceleration, the magnetic field, and the total energy density, respectively, \mathbf{I} is a unit tensor, η is the resistivity, $\mathbf{j} = \nabla \times \mathbf{B}$ is the current density, and p_t represents the total (thermal and magnetic) pressure defined as

$$p_t = p + \frac{B^2}{2}. \quad (6)$$

The thermal pressure p is given by

$$p = (\gamma - 1) \left(e - \frac{1}{2} \rho v^2 - \frac{B^2}{2} \right), \quad (7)$$

where γ is the specific heat ratio.

The equation (5) for ψ with equation (3) is introduced so that the solenoidal property of the magnetic field

$$\nabla \cdot \mathbf{B} = 0 \quad (8)$$

is maintained within minimal errors during time integration (see subsection 2.4). The equations (1) – (5) complete a set of the MHD equations, which is conventionally referred to as GLM–MHD equations (Dedner et al. 2002).

The GLM–MHD equations then read

$$\frac{\partial \mathbf{U}}{\partial t} + \sum_{s=x,y,z} \frac{\partial \mathbf{F}_s}{\partial s} = \mathbf{S} \quad (9)$$

where

$$\mathbf{U} = \begin{pmatrix} \rho & \rho \mathbf{v} & \mathbf{B} & e & \psi \end{pmatrix}^T \quad (10)$$

is a state vector of the conservative variables,

$$\mathbf{F}_s = \begin{pmatrix} \rho v_s \\ \rho v_s \mathbf{v} + p_T \mathbf{I} - B_s \mathbf{B} \\ v_s \mathbf{B} - B_s \mathbf{v} + \psi \mathbf{I} \\ (e + p_T) v_s - B_s (\mathbf{v} \cdot \mathbf{B}) \end{pmatrix}, \quad (11)$$

is a flux vector, and

$$\mathbf{S} = \begin{pmatrix} 0 & \rho \mathbf{g} & -\nabla \times (\eta \mathbf{j}) & -\nabla \cdot (\eta \mathbf{j} \times \mathbf{B}) + \rho \mathbf{v} \cdot \mathbf{g} & -\frac{c_h^2}{c_p^2} \psi \end{pmatrix}^T, \quad (12)$$

is a source vector. We also define a vector \mathbf{V} for the primitive variables

$$\mathbf{V} = \begin{pmatrix} \rho & \mathbf{v} & \mathbf{B} & p & \psi \end{pmatrix}^T. \quad (13)$$

Let us consider equation (9) with $\mathbf{S} = 0$ in one dimension (1D) ($s = x$). It can be written in the form

$$\frac{\partial \mathbf{U}}{\partial t} + A \frac{\partial \mathbf{U}}{\partial x} = \frac{\partial \mathbf{V}}{\partial t} + A_p \frac{\partial \mathbf{V}}{\partial x} = 0, \quad (14)$$

where

$$A = \frac{\partial \mathbf{F}_x}{\partial \mathbf{U}} \quad (15)$$

and

$$A_p = \left(\frac{\partial \mathbf{U}}{\partial \mathbf{V}} \right)^{-1} A \frac{\partial \mathbf{U}}{\partial \mathbf{V}} \quad (16)$$

are the Jacobian matrix for the conservative and the primitive variables, respectively, and

$$\frac{\partial \mathbf{U}}{\partial \mathbf{V}} = \begin{pmatrix} 1 & 0 & 0 & 0 & 0 \\ \mathbf{v} & \rho & 0 & 0 & 0 \\ 0 & 0 & 1 & 0 & 0 \\ \frac{\mathbf{v} \cdot \mathbf{v}}{2} & \rho \mathbf{v} & \mathbf{B} & \frac{1}{\gamma-1} & 0 \\ 0 & 0 & 0 & 0 & 1 \end{pmatrix} \quad (17)$$

is the quasilinear conversion matrix, which relates $\delta \mathbf{V}$ to $\delta \mathbf{U}$. Multiplying equation (14) by the left eigenvector (\mathbf{L}_p with $\mathbf{L}_p \mathbf{R}_p = \mathbf{I}$) of the Jacobian matrix gives the equation for the characteristic variables \mathbf{W} as

$$\mathbf{L}_p \frac{\partial \mathbf{V}}{\partial t} + \mathbf{L}_p A_p \mathbf{R}_p \mathbf{L}_p \frac{\partial \mathbf{V}}{\partial x} = \frac{\partial \mathbf{W}}{\partial t} + \Lambda \frac{\partial \mathbf{W}}{\partial x} = 0, \quad (18)$$

where $\delta \mathbf{W} = \mathbf{L}_p \delta \mathbf{V}$, and $\mathbf{L}_p A_p \mathbf{R}_p = \Lambda = \text{diag}(\lambda_1, \lambda_2, \dots, \lambda_9)$ is a diagonal matrix containing the eigenvalues. For the GLM-MHD equations, $\lambda_1 \sim \lambda_9$ are

$$\lambda_{1,9} = \mp c_h, \quad \lambda_{2,8} = v_x \mp c_f, \quad \lambda_{3,7} = v_x \mp c_a, \quad \lambda_{4,6} = v_x \mp c_s, \quad \lambda_5 = v_x, \quad (19)$$

where

$$c_{f,s} = \left(\frac{\gamma p + |\mathbf{B}|^2 \pm \sqrt{(\gamma p + |\mathbf{B}|^2)^2 - 4\gamma p B_x^2}}{2\rho} \right)^{1/2} \quad (20)$$

refer to the fast (positive) and slow (negative) magnetosonic speeds, respectively, and

$$c_a = \frac{|B_x|}{\sqrt{\rho}} \quad (21)$$

is the Alfvén speed. In addition to the fast ($\lambda_{2,8}$), the Alfvén ($\lambda_{3,7}$), the slow ($\lambda_{4,6}$), and the entropy (λ_5) waves of the ideal MHD system, the GLM-MHD system introduces two waves with the eigenvalues (phase speeds) of $\lambda_{1,9} = \mp c_h$, which represent omnidirectional propagation of numerical errors of the

divergence-free condition (equation (8)).

2.2 Numerical algorithms

Time evolution of the equation (9) for the state vector at a cell $\mathbf{U}_{i,j,k}$ is obtained by the finite volume method

$$\frac{\partial \bar{\mathbf{U}}_{(i,j,k)}}{\partial t} = - \sum_{s=i,j,k} \frac{\mathbf{F}_{(s+1/2)}^* - \mathbf{F}_{(s-1/2)}^*}{\Delta_s} + \mathbf{S}_{(i,j,k)} \equiv L(\bar{\mathbf{U}}), \quad (22)$$

where $\bar{\mathbf{U}}$ is the cell-averaged value of \mathbf{U} , Δ_s with $s = i, j, k$ represents cell width in each dimension, $\mathbf{F}_{(s\pm 1/2)}^*$ denotes a numerical flux at cell surfaces, and $L(\bar{\mathbf{U}})$ defines a numerical operator of the finite volume method. Equation (22) is integrated with time by the third-order strong-stability-preserving (SSP) Runge–Kutta scheme (Suresh and Huynh 1997; Gottlieb and Shu 1998):

$$\mathbf{u}^{(0)} = \bar{\mathbf{U}}^n, \quad (23)$$

$$\mathbf{u}^{(1)} = \mathbf{u}^{(0)} + \Delta t^n L(\mathbf{u}^{(0)}), \quad (24)$$

$$\mathbf{u}^{(2)} = \frac{3}{4}\mathbf{u}^{(0)} + \frac{1}{4}\left(\mathbf{u}^{(1)} + \Delta t^n L(\mathbf{u}^{(1)})\right), \quad (25)$$

$$\mathbf{u}^{(3)} = \frac{1}{3}\mathbf{u}^{(0)} + \frac{2}{3}\left(\mathbf{u}^{(2)} + \Delta t^n L(\mathbf{u}^{(2)})\right), \quad (26)$$

$$\bar{\mathbf{U}}^{n+1} = \mathbf{u}^{(3)}, \quad (27)$$

where the superscript n stands for a number of time steps and Δt^n is a corresponding step size. Δt^n is determined from the Courant–Friedrichs–Lewy (CFL) condition

$$\Delta t = \sigma_c \min_{i,j,k} \left(\frac{\Delta_i}{\max(|\lambda_{i2}|, |\lambda_{i8}|)}, \frac{\Delta_j}{\max(|\lambda_{j2}|, |\lambda_{j8}|)}, \frac{\Delta_k}{\max(|\lambda_{k2}|, |\lambda_{k8}|)} \right), \quad (28)$$

where $\lambda_{s2,8}$ ($s = i, j, k$) is the eigenvalue for the fast magnetosonic wave calculated for each dimension, and σ_c is the CFL number. For the resistive MHD case, i.e., $\eta \neq 0$, Δt from equation (28) is again compared with the one determined from the diffusion number σ_d

$$\Delta t = \min \left(\Delta t, \sigma_d \min_{i,j,k} \left(\frac{\Delta_i^2}{\eta_{(i,j,k)}}, \frac{\Delta_j^2}{\eta_{(i,j,k)}}, \frac{\Delta_k^2}{\eta_{(i,j,k)}} \right) \right). \quad (29)$$

In the following numerical experiments, $\sigma_c = \sigma_d = 0.3$ were adopted unless otherwise stated.

The numerical operator $L(\bar{\mathbf{U}})$ is evaluated by following procedures.

1. Conversion from the cell-averaged primitive variables to the characteristic variables locally (Harten et al. 1987). This operation is done by multiplying the primitive variables at cells within a stencil centered at a cell (i, j, k) by the left eigenvector calculated at the cell (i, j, k) . For example, in the x -direction,

$$\mathbf{W}_{(i+q,j,k)} = \mathbf{L}_{p(i,j,k)} \bar{\mathbf{V}}_{(i+q,j,k)} \quad (30)$$

with q varying from $-r$ to $+r$ for the $(2r + 1)$ th-order scheme. Among various eigenvectors, CANS+ adopts the same eigenvectors as those used in the Athena code (Stone et al. 2008). Although this conversion is computationally expensive, separating waves according to the characteristics is necessary for obtaining nonoscillatory profiles by higher-order reconstructions as in the following.

2. Reconstruction of the characteristic variables \mathbf{W} within a cell. To obtain high-resolution, non-oscillatory profiles, the fifth-order-monotonicity-preserving (MP5) interpolation scheme (Suresh and Huynh 1997) is used (see subsection 2.3). In the MP5 scheme, a five-point stencil ($r = 2$) is required for the conversion and the reconstruction steps. The interpolated values at both cell surfaces are obtained at once in each dimension. For example, for a cell at (i, j, k) in the x-direction, the left-hand, right-state vector ${}^R\mathbf{W}_{(i-1/2, j, k)}$ and the right-hand, left-state vector ${}^L\mathbf{W}_{(i+1/2, j, k)}$ can be obtained for each interpolation procedure.
3. The interpolated values at cell surfaces are then converted to the primitive variables using the local right eigenvector as

$${}^R\mathbf{V}_{(i-1/2, j, k)} = \mathbf{R}_{px(i, j, k)} {}^R\mathbf{W}_{(i-1/2, j, k)}, \quad (31)$$

$${}^L\mathbf{V}_{(i+1/2, j, k)} = \mathbf{R}_{px(i, j, k)} {}^L\mathbf{W}_{(i+1/2, j, k)}, \quad (32)$$

$${}^R\mathbf{V}_{(i, j-1/2, k)} = \mathbf{R}_{py(i, j, k)} {}^R\mathbf{W}_{(i, j-1/2, k)}, \quad (33)$$

$${}^L\mathbf{V}_{(i, j+1/2, k)} = \mathbf{R}_{py(i, j, k)} {}^L\mathbf{W}_{(i, j+1/2, k)}, \quad (34)$$

$${}^R\mathbf{V}_{(i, j, k-1/2)} = \mathbf{R}_{pz(i, j, k)} {}^R\mathbf{W}_{(i, j, k-1/2)}, \quad (35)$$

$${}^L\mathbf{V}_{(i, j, k+1/2)} = \mathbf{R}_{pz(i, j, k)} {}^L\mathbf{W}_{(i, j, k+1/2)}, \quad (36)$$

where \mathbf{R}_{ps} with $s = x, y, z$ represents the right eigenvector in each direction.

4. Evaluation of the numerical flux \mathbf{F}^* in each dimension by the Godunov-type scheme. That is, the numerical flux at a cell surface $(i + 1/2, j, k)$, for example, can be obtained from

$$\mathbf{F}_{i+1/2}^* = \mathbf{F}(\bar{\mathbf{U}}_i^n) - \frac{1}{\Delta t^n} \int_{x_i}^{x_{i+1/2}} \mathbf{U}_R \left(\frac{x - x_{i+1/2}}{\Delta t}; {}^L\mathbf{V}_{i+1/2}, {}^R\mathbf{V}_{i+1/2} \right) dx + \frac{x_{i+1/2} - x_i}{\Delta t^n} \bar{\mathbf{U}}_i^n, \quad (37)$$

where $\mathbf{U}_R \left(\frac{x - x_{i+1/2}}{\Delta t}; {}^L\mathbf{V}_{i+1/2}, {}^R\mathbf{V}_{i+1/2} \right)$ is a solution inside the Riemann fan during a time interval of Δt with the initial conditions of the left (${}^L\mathbf{V}_{i+1/2}$) and right (${}^R\mathbf{V}_{i+1/2}$) states. (Here we have omitted (j, k) in the notations for simplicity.) CANS+ employs the HLLD approximate Riemann solver of Miyoshi and Kusano (2005), which gives accurate and robust solutions to Riemann problems. Note, however, that equations for the magnetic field component normal to the cell surface and for ψ are decoupled from the seven remaining equations. The numerical flux values for these variables are easily obtained separately (see subsection 2.4).

5. The source term is evaluated at each Runge–Kutta substage (equations (24) – (26)).

6. Conversion from the updated conservative variables to the primitive variables.
7. Return to 1.

2.3 The MP5 scheme

The MP5 scheme in the reconstruction step is based on a fourth-degree polynomial for each dimension. The left state of a quantity f at a cell $i + 1/2$ is first evaluated by

$$^L f_{i+1/2} = \frac{2\bar{f}_{i-2} - 13\bar{f}_{i-1} + 47\bar{f}_i + 27\bar{f}_{i+1} - 3\bar{f}_{i+2}}{60}, \quad (38)$$

where \bar{f} is a cell-averaged value of f . The right state at $i - 1/2$ is also obtained at the same time from its symmetry in each dimension:

$$^R f_{i-1/2} = \frac{2\bar{f}_{i+2} - 13\bar{f}_{i+1} + 47\bar{f}_i + 27\bar{f}_{i-1} - 3\bar{f}_{i-2}}{60}. \quad (39)$$

The original value results in a fifth-order spatially accurate solution in smooth regions, but an oscillatory profile around discontinuities. The MP5 scheme seeks a profile that degrades to the first order only around discontinuities. For this purpose, the original value is then brought to an interval using the median function

$$^L f_{i+1/2} = \text{median}(^L f_{i+1/2}, f_{min}, f_{max}). \quad (40)$$

Here the median function returns an intermediate value among three variables in the arguments, so that the cell surface value lies in an interval between f_{min} and f_{max} . The basic concept is therefore the same as in standard TVD schemes. The TVD schemes with a three-point stencil, however, cannot distinguish between a discontinuity and a smooth profile around the extremum (figure 1). The interpolated value around the extremum of a sinusoidal profile (figure 1(a)) is then bounded by the neighboring cell values, resulting in strong damping of the waveform (figure 1(b)). Because of this difficulty, the TVD schemes have been applied mainly to problems where strong shock waves dominate. Accuracy and monotonicity preservation of profiles are accomplished in the MP5 scheme by using two additional values at cells (open circles in figure 1) to distinguish between the two. The curvature of a profile can be calculated by using the five-point stencil, and the interval is expanded in cases when the profile is identified as parabola. Analytic consideration of the monotonicity preservation under the SSP Runge–Kutta time integration for a linear advection equation leads to a CFL number restriction $\sigma_c < 0.2$ in the MP5 scheme. In practice, $\sigma_c = 0.3$, which was adopted in the following numerical tests, still gives nonoscillatory results. Readers may consult the original article by Suresh and Huynh (1997) for detailed derivations of f_{min} and f_{max} , and the CFL restriction.

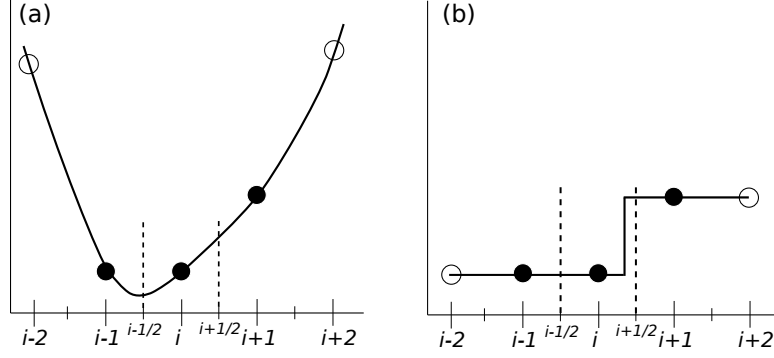


Fig. 1. Profile reconstructions around a cell i using different numbers of stencils (filled and open circles) for (a) parabola and (b) stair-step profiles. Vertical dashed lines indicate cell boundaries where reconstructed data are needed. This figure is adapted from figure 2.1 in Suresh and Huynh (1997)

2.4 Hyperbolic divergence cleaning method

Upwind schemes including the finite volume method always suffer from numerical errors of the solenoidal property of the magnetic field. This occurs because the Lorentz force term in the momentum equation (equation (2)) involves an acceleration term along the magnetic field arising from numerical errors of $\nabla \cdot \mathbf{B}$; that is,

$$-\nabla \cdot \left(\frac{|\mathbf{B}|^2}{2} \mathbf{I} - \mathbf{B}\mathbf{B} \right) = (\nabla \times \mathbf{B}) \times \mathbf{B} + \mathbf{B}(\nabla \cdot \mathbf{B}), \quad (41)$$

which finally leads to undesired results and thus inhibits following the long-term evolution of multidimensional problems. To overcome this inherent problem in multidimensional MHD simulations, several approaches have been developed (Toth 2000; Miyoshi and Kusano 2011). Among them, modern MHD simulation codes have adopted strategies to satisfy discretized forms of the divergence-free condition within machine round-off errors based on a family of upwind constrained-transport (CT) algorithms (Londrillo and Del Zanna 2004; Gardiner and Stone 2005; Mignone et al. 2007; Lee and Deane 2009; Miyoshi and Kusano 2011; Minoshima et al. 2015). In contrast, CANS+ adopts the hyperbolic divergence cleaning method (Dedner et al. 2002; Mignone et al. 2010), which transports and damps numerical errors of the divergence-free condition, so that the growth of errors is managed to be within minimal levels. More specifically, multiplying the equation (5) by $\partial/\partial t$ and equation (3) by $\nabla \cdot$, one finds that the scalar potential ψ and $\nabla \cdot \mathbf{B}$ obey the telegraph equations

$$\frac{\partial^2 \psi}{\partial t^2} + \frac{c_h^2}{c_p^2} \frac{\partial \psi}{\partial t} - c_h^2 \nabla^2 \psi = 0, \quad (42)$$

$$\frac{\partial^2 (\nabla \cdot \mathbf{B})}{\partial t^2} + \frac{c_h^2}{c_p^2} \frac{\partial (\nabla \cdot \mathbf{B})}{\partial t} - c_h^2 \nabla^2 (\nabla \cdot \mathbf{B}) = 0, \quad (43)$$

where c_h and c_p are constants, and characterize the propagation speed and the damping rate, respectively.

Equation (5) has a semiconservative form and thus its numerical solution can benefit from the same high-order scheme applied to the original MHD equations. Let us consider the corresponding equations:

$$\frac{\partial}{\partial t} \begin{pmatrix} B_s \\ \psi \end{pmatrix} + \begin{pmatrix} 0 & 1 \\ c_h^2 & 0 \end{pmatrix} \begin{pmatrix} \nabla \cdot \mathbf{B} \\ \partial \psi / \partial s \end{pmatrix} = \begin{pmatrix} 0 \\ -\frac{c_h^2}{c_p^2} \psi \end{pmatrix}. \quad (44)$$

The system equations without the source term on the right-hand side in each dimension are decoupled from the MHD equations, and have eigenvalues of $\lambda_{1,9} = \mp c_h$ and the right eigenvectors of $(1 \pm c_h)^T$. As c_h is a constant, they are linear equations. Thus, the numerical flux at a cell surface is given as

$$\mathbf{F}_s^* = \begin{pmatrix} \psi^* \\ c_h^2 B_s^* \end{pmatrix} = \begin{pmatrix} \frac{1}{2}(^R \psi + ^L \psi) - \frac{c_h}{2}(^R B_s - ^L B_s) \\ \frac{c_h^2}{2}(^R B_s + ^L B_s) - \frac{c_h}{2}(^R \psi - ^L \psi) \end{pmatrix}, \quad (45)$$

where $^L \psi$, $^L B_s$, $^R \psi$, and $^R B_s$ denote the left (L) and the right (R) states at the cell surface for each quantity, respectively. These can be obtained in the same manner as in the reconstruction step. The obtained numerical flux is added to the numerical flux from the HLLD Riemann solver.

The contribution from the source term $(0 \ -\psi c_h^2/c_p^2)^T$ is then added in an operator-split fashion as

$$\psi^{(m)} = C_1^{(m)} \psi^{(0)} + C_2^{(m)} \left(\psi^{(m-1)} + \Delta t^n L_{FV}(\psi^{(m-1)}) \right) \exp \left(-\frac{c_h^2}{c_p^2} \Delta t^n \right), \quad (46)$$

where C_1 and C_2 are the weighting coefficients, L_{FV} represents the finite volume differentiation in equation (44), and the superscripts on ψ , C_1 , and C_2 denote the Runge–Kutta substage (m) in equations (23)–(26).

The constants of c_h and c_p can be arbitrary defined. As c_h represents the propagation speed of numerical errors, it is typically determined from the CFL condition as

$$c_h = \min_{i,j,k} (\Delta_i, \Delta_j, \Delta_k) \frac{\sigma_c}{\Delta t^n}. \quad (47)$$

Then, c_p is determined from the relation $c_p^2/c_h = \text{const.}$ so as to equal the transport and decay time scales. Numerical experiments have shown that $c_p = \sqrt{0.18} c_h$ results in the best performance regardless of grid resolution (Dedner et al. 2002) and was adopted in CANS+.

2.5 Some prescriptions for numerical stability

Higher-order, multidimensional codes usually suffer from vanishing and negative values of the scalar variables (ρ and p). CANS+ ensures numerical stability by examining the following prescriptions.

- In the reconstruction step, the first-order interpolation is applied for the scalar variables and the

normal component of the vector fields:

- if one of the scalar variables recovered from the interpolated characteristic variables at a cell surface resulted in a negative value, or
- if one of the scalar variables at a cell centered in the five-point stencil was two orders of magnitude smaller than the other cell values.
- In the conversion step, the thermal pressure given by the equation (7) is evaluated every time in the Runge–Kutta substage. If the pressure becomes negative, it is overwritten by the value in the previous substage. The pressure is also evaluated in terms of the plasma beta ($\beta = 2p/B^2$) so as to bound the minimum β value. CANS+ allows $\beta \geq \beta_{min} = 0.001$. The total energy density is then updated by the new pressure value. Thus, it is not strictly conserved in CANS+, while the mass conservation is satisfied.

These operations can provide stable solutions in rarefied and low- β plasma regions as demonstrated in the two-dimensional (2D) simulations of the Parker instability as will be shown in 3.2.3.

2.6 CANS+ in cylindrical coordinates

CANS+ in cylindrical coordinates is straightforwardly implemented by converting the notations of $(\partial x, \partial y, \partial z)$ to $(\partial r, r\partial\phi, \partial z)$, and adding the remaining terms

$$\mathbf{F}_{cyl} = \begin{pmatrix} -\frac{F_r}{r} \\ -\frac{1}{r} \left[\rho(v_r^2 - v_\phi^2) - (B_r^2 - B_\phi^2) \right] \\ -\frac{2F_\phi}{r} \\ -\frac{F_r}{r} \\ 0 \\ 0 \\ -\frac{F_\phi}{r} \\ -\frac{F_r}{r} \\ -\frac{F_r}{r} \end{pmatrix} \quad (48)$$

to the source term of equation (12). Whereas the v_r -component of \mathbf{F}_{cyl} is evaluated by the primitive variables directly, the other components are calculated by averaging the numerical flux at the cell center. This version of the code has been used in global simulations of accretion disks as will be shown in Section 4.

3 Code Assessments

In this section, we present results from numerical tests to assess CANS+ by comparing with results from the second-order MUSCL scheme with the monotonized central (MC) limiter. For specific heat ratio, gravity, and resistivity, $\gamma = 5/3$, $g = 0$, and $\eta = 0$ were adopted in the following tests unless otherwise stated.

3.1 One-dimensional problems

3.1.1 Alfvén wave propagation

The spatial resolution of the MP5 scheme in CANS+ was verified by 1D tests of circularly polarized Alfvén wave propagations with various numbers of computational cells per wavelength. We initially set the magnetic and velocity profiles as

$$\begin{aligned} B_x &= B_0, \\ B_y &= 0.1B_0 \cos(2\pi x), \\ B_z &= 0.1B_0 \sin(2\pi x), \\ V_y &= -B_y, \\ V_z &= -B_z, \end{aligned}$$

where we have used units of the system size $L_x = 1$, the background Alfvén speed $V_{A0} = 1$, and the Alfvén transit time $T_0 = L_x/V_{A0}$. The CFL number $\sigma_c = 0.05$ was adopted to minimize errors from time integrations in the following analyses on spatial resolutions.

Figure 2(a) shows spatial profiles of B_z obtained by the CANS+ (red) and the MUSCL scheme (blue). The wavelength is resolved with 16 cells. After five Alfvén transit times ($t = 5$), while the amplitude of the wave has decreased by 25% in the MUSCL scheme, the profile from the MP5 scheme almost overlapped the theoretical profile (black). This strong damping of the wave is an inherent property of the TVD schemes. In contrast, the MP5 scheme can detect smooth profiles and thus give a high-resolution result without modifying the original profile.

Numerical experiments with various cell widths gave orders of accuracy of the schemes. Figure 2(b) shows L_1 norms of the numerical errors from the MP5 (red) and the MUSCL (blue) schemes. The numerical errors increased with cell width according to the degree of the interpolation polynomial of each scheme. As expected, the dashed lines indicate that the MUSCL and the MP5 schemes have the second- ($\propto \Delta x^2$) and fifth-order ($\propto \Delta x^5$) accuracies in space, respectively.

It is also worth pointing out that the numerical errors are much larger in the MUSCL scheme than in the MP5 scheme when compared at the same cell size (figure 2(b)). In other words, the MP5

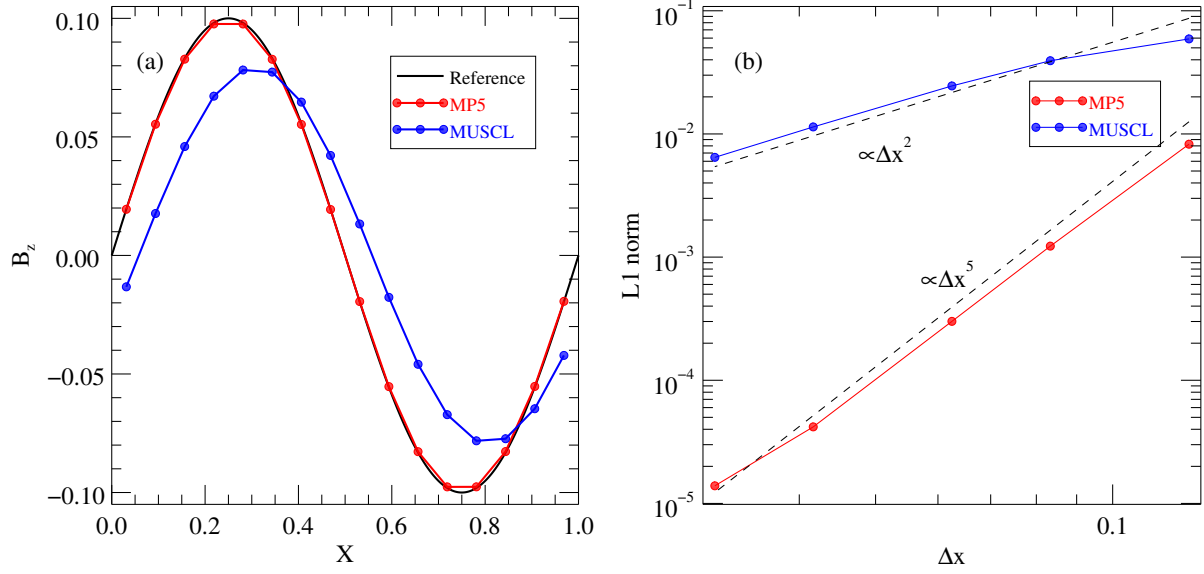


Fig. 2. Circularly polarized linear Alfvén wave propagation tests from MP5 (red) and MUSCL (blue) schemes. (a) B_z profiles after five Alfvén transit times ($t=5$). The black curve indicates the analytic position of the wave. (b) L_1 norm errors obtained from numerical experiments with different grid resolutions. Dashed lines indicate the order of accuracy in space.

scheme can provide numerical solutions at the same accuracy with much coarser cells than those required in the MUSCL scheme. This has great benefits for saving numerical costs, because they increase as $\Delta x^{-(n+1)}$ in n -dimensional simulations, while the number of numerical operations in the MP5 scheme increases by only a few times.

3.1.2 Shock tube problem

The monotonicity preservation of CANS+ was verified by a standard shock tube problem (Brio and Wu 1988; Ryu and Jones 1995). We initially set for this shock tube problem the values $(\rho, p, V_x, V_y, V_z, B_x, B_y, B_z)_L = (1, 1, 0, 0, 0, 0.75, 1, 0)$ in a region on the left-hand side of the simulation domain, $0 \leq x < 0.5$, and $(\rho, p, V_x, V_y, V_z, B_x, B_y, B_z)_R = (0.125, 0.1, 0, 0, 0, 0.75, -1, 0)$ on the right-hand side in $0.5 \leq x \leq 1$ with $\gamma = 5/3$ (Ryu and Jones 1995). We used 512 computational cells for this problem.

Figure 3(a) and 3(d) respectively show ρ and V_x profiles at $t = 0.1$ obtained by CANS+ (red), and we compared them with the MUSCL scheme (blue) and the reference result obtained by the first-order scheme with 8192 cells (black). Characteristic profiles (from left to right: fast rarefaction, slow compound, contact discontinuity, slow shock, and fast rarefaction) were reproduced by CANS+. In particular, the contact discontinuity ($x \sim 0.56$) and the slow shock wave ($x \sim 0.63$) were resolved more sharply (figure 3(b) and 3(e)) than in the MUSCL scheme. A staircasing profile around the compound wave in the CANS+ is the inherent property of the MP5 scheme (Suresh and Huynh 1997).

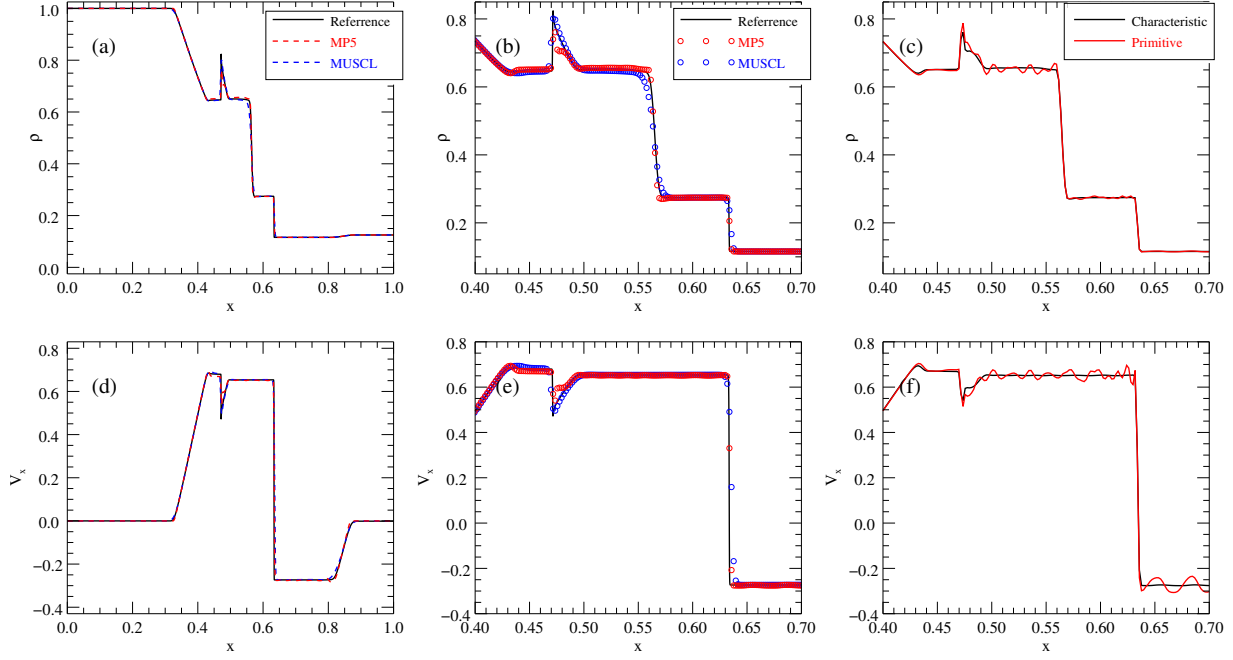


Fig. 3. Brio & Wu's shock tube problem: (a) and (b) show the mass density and (d) and (e) the x -component of velocity profiles for the MP5 (red) and MUSCL (blue) schemes. The reference result (black) is obtained by the first-order scheme using 8192 cells. Enlarged views of the mass density and velocity profiles are shown in (b) and (e), respectively. (c) and (f) compare the differences in mass density and velocity profiles arising from the MP5 reconstructions based on the characteristic (black) and primitive (red) variables.

Figure 3(c) and 3(f) compare the results from the MP5 scheme with different variables for the interpolation to cell surfaces. The reconstruction of the characteristic variables (black) that was used in CANS+ resulted in the best performance to capture the discontinuities among other variables used for the reconstruction, including the primitive variables shown in the figure (red). Interpolation of the characteristic variables, which were actually transported by the waves, was necessary for obtaining nonoscillatory results with the present fifth-order scheme.

3.2 2D problems

3.2.1 The Kelvin–Helmholtz instability

Evolutions of the Kelvin–Helmholtz (K–H) instability in inhomogeneous plasma are presented as a multidimensional problem. We initially set the velocity shear profile as $V_x = -0.5V_0 \tanh(y/\lambda)$, where V_0 was 1.6 times the Alfvén speed V_A , λ was the half thickness of the velocity shear layer, and the mass density profile was set as $\rho = 0.5\rho_0 [(1 - \alpha) \tanh(y/\lambda) + 1 + \alpha]$ with $\alpha = 0.1$. The magnetic field has only an out-of-plane component $\mathbf{B} = (0, 0, B_0)$. The system size in the x -direction (L_x) is equal to the wavelength of the fastest growing mode ($L_x = 11.2\lambda$) obtained by the linear analysis for the present initial conditions (Matsumoto and Seki 2010). The system size in the y -

direction (L_y) was in the range $-10\lambda \leq y \leq 10\lambda$ ($L_y = 20\lambda$). With these initial configurations, we added a sinusoidal perturbation to the y component of the velocity inside the shear layer as $\delta V_y = 0.01V_0 \sin(2\pi x/L_x) \cosh^{-2}(y/\lambda)$. Quantities were normalized to V_A , B_0 , ρ_0 , λ , and λ/V_0 . λ was resolved with 32 cells. This initial configuration allowed us to benchmark the code's capability of capturing hydrodynamical turbulence along with the contact discontinuity.

Figure 4 shows the mass density profiles taken during nonlinear evolution with the MP5 (figure 4(a) and 4(d)) and the MUSCL (figure 4(e)) schemes. Saturated K–H billows naturally formed sharp contact discontinuities, which eventually broke into turbulence via the secondary K–H and Rayleigh–Taylor instabilities (Matsumoto and Hoshino 2004). The unstable mode grew exponentially as expected from the linear analysis (figure 4(b)) in both results from the MP5 (solid) and MUSCL (dash–dot) schemes, whereas different behaviors in the nonlinear stage can be found in $t > 70$. A sharp mass density profile at $x = 8.4$ in the y -direction at $t = 55$ (figure 4(c)) verified that the MP5 scheme was capable of capturing the contact discontinuity and development of small-scale eddies at the same time precisely. Further development of the K–H turbulence contrasted the overall mixing efficiency between different schemes. The MP5 scheme allowed the kinetic energy to be cascaded to small-scale vortices (figure 4(d) and 4(f)), whereas the MC limiter adopted in the MUSCL scheme dissipated the cascaded energy at scales much larger than the cell size (figure 4(e) and 4(f)).

3.2.2 The Orszag–Tang vortex

We present results of the so-called Orszag–Tang vortex problem (Orszag and Tang 1979) to test the code's capability of capturing shock–shock interactions and turbulence. We initiated the problem with $(\rho, p, V_x, V_y, V_z, B_x, B_y, B_z) = (\gamma^2, \gamma, -\sin(x), \sin(x), 0, -\sin(y), \sin(2x), 0)$ in the simulation domain of $0 \leq x, y \leq 2\pi$. The periodic boundary condition was applied in the x - and y -directions. 200×200 cells were used to compare the results from the MP5 and MUSCL schemes. Results with 800×800 cells by the MUSCL scheme are also given as a reference run.

Figure 5 shows temperature ($T = P/\rho$) profiles from the MP5 (figure 5(a)) and the MUSCL schemes (figure 5(b)). The overall structures seem to overlap with each other as characterized by sharp discontinuities at shock waves. Besides the overall structure, a closer look at the profile along the x -direction at $y = 0.5\pi$ (figure 5(c) and the inset) shows that a fine-scale structure ($x \sim 0.75$) was well resolved by the MP5 scheme (red filled circles) overlapping the reference run (black curve) compared with the MUSCL scheme (blue filled circles).

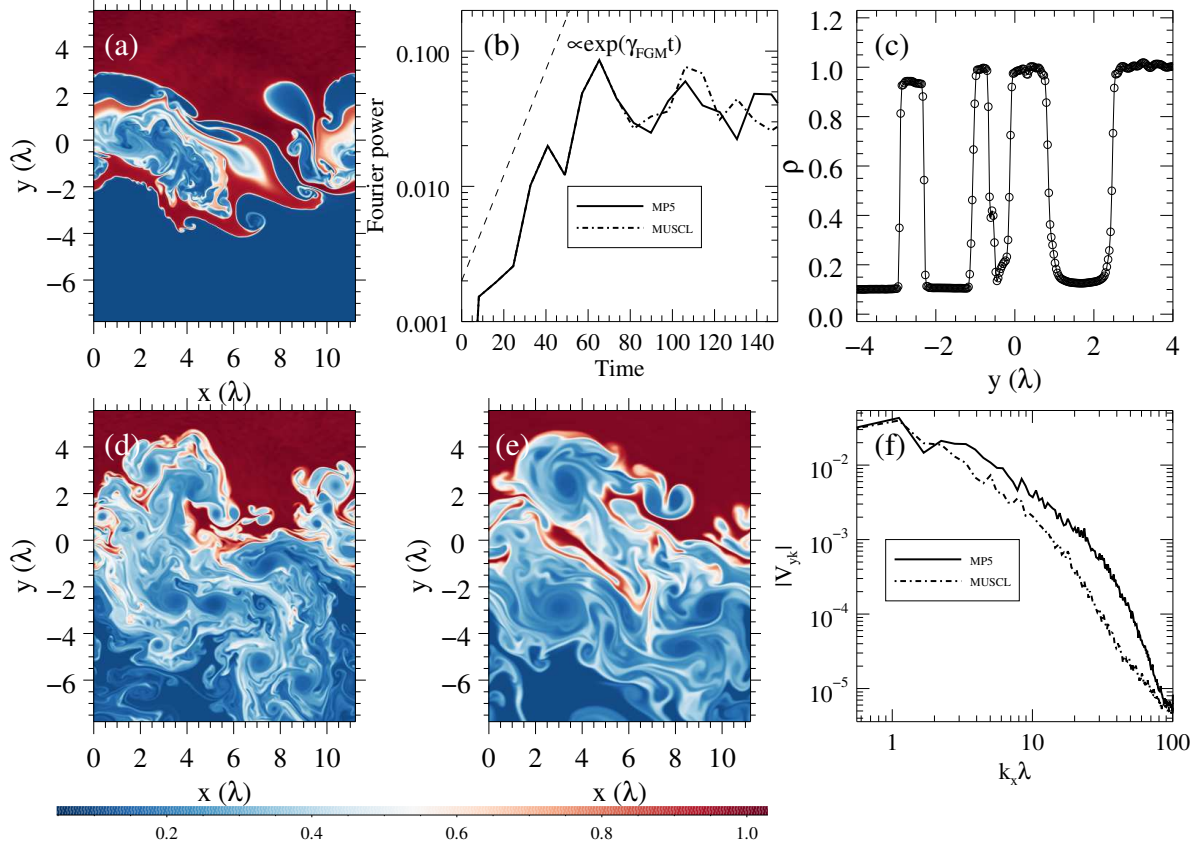


Fig. 4. Evolutions of the Kelvin-Helmholtz instability. (a) Mass density profile in the late linear growth phase at $t = 55$. (b) Time evolutions of the Fourier amplitude of the fastest growing mode of V_y from the MP5 (solid line) and MUSCL (dash-dot line) schemes. The dashed line indicates the linear growth rate obtained by Matsumoto and Seki (2010). (c) Mass density profile from the MP5 run in the y -direction at $x = 8.4$, $t = 55$. Mass density profiles from the (d) MP5 and (e) MUSCL schemes after the transition to turbulence at $t = 95$. (f) Spectra of the y component of the velocity in the x -direction averaged over the simulation domain at $t = 95$ for the MP5 (solid line) and MUSCL (dash-dot line) schemes.

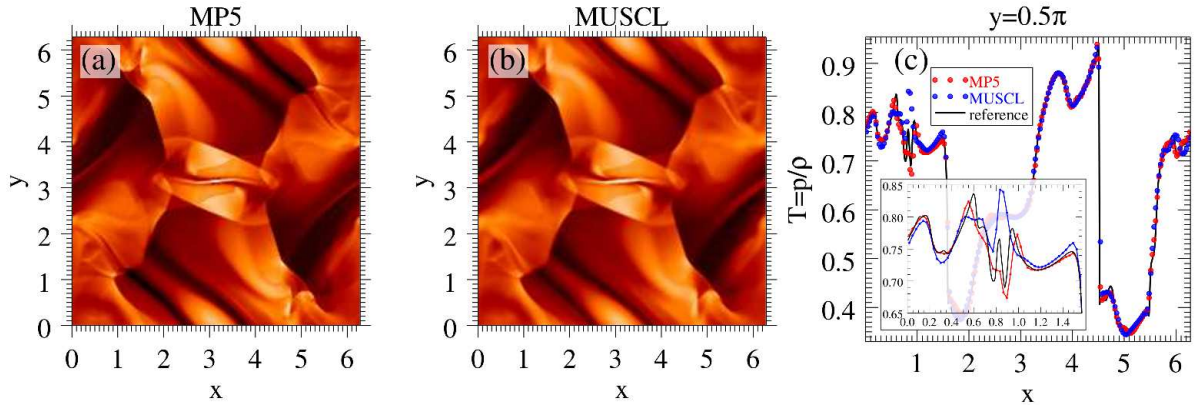


Fig. 5. The Orsarg-Tang vortex problem. Temperature ($T = p/\rho$) profiles at $t = 0.2\pi$ are shown for the (a) MP5 and (b) MUSCL schemes. (c) The profiles in the x -direction at $y = 0.5\pi$ are compared between the MP5 (red circle) and MUSCL (blue circle) schemes along with the result from the high-resolution run (800×800 cells) with the MUSCL scheme (black curve) as a reference. The inset shows an enlarged view in $0 < x < 0.5\pi$.

3.2.3 Parker instability

Magnetized plasma stratified under the gravity becomes destabilized as a result of the buoyancy force against the magnetic tension force. This instability is known as the Parker instability (Parker 1966), and its nonlinear evolution is characterized by bent magnetic field lines in rarefied plasma (Matsumoto et al. 1988). We chose this problem as a benchmark test for evaluating the code's capability of solving low- β plasma in multidimensions. In the present test, the gravity acceleration term \mathbf{g} on the right-hand side of equation (2) was retained.

The Parker instability was initialized with the gravity acceleration profile

$$\mathbf{g} = \left(0, -g_0 \tanh\left(\frac{y}{H_g}\right) \right), \quad (49)$$

and the temperature

$$T = T_0 + \frac{1}{2}(T_1 - T_0) \left[\tanh\left(\frac{|y| - y_0}{H_t}\right) + 1 \right]. \quad (50)$$

The mass density was determined from the static equilibrium

$$\frac{d}{dy} \left[(1 + \beta_0^{-1}) p \right] = \rho g, \quad (51)$$

where β_0 is the ratio of the thermal pressure to the magnetic pressure, and $p = \rho T / \gamma$. The magnetic field has only the x -component (B_x) with strength given by the plasma beta β_0 . The spacial length, velocity, and time were normalized to the scale height H_0 , the sound speed C_{s0} at $y = 0$, and the transit time H_0 / C_{s0} , respectively. Other quantities such as g , ρ , p , T , and B_x were normalized to C_{s0}^2 / H_0 , ρ_0 , $\rho_0 C_{s0}^2$, $C_{s0}^2 / (\gamma / m)$, and $\sqrt{\rho_0 C_{s0}^2}$, respectively. We adopted $\gamma = 1.05$, $g_0 = 1.47$, $H_g = 5.0$, $H_t = 0.5$, $y_0 = 10.0$, $T_0 = 1$, $T_1 = 25$, and $\beta_0 = 1.0$.

With these initial configurations, we added a perturbation to V_x in an antisymmetric form with respect to the $y = 0$ plane as

$$\delta V_x = 0.05 \sin\left(\frac{2\pi x}{\lambda}\right) \times \left[+ \left\{ \tanh\left(\frac{y + y_2}{H_{pt}}\right) - \tanh\left(\frac{y + y_3}{H_{pt}}\right) \right\} - \left\{ \tanh\left(\frac{y - y_2}{H_{pt}}\right) - \tanh\left(\frac{y - y_3}{H_{pt}}\right) \right\} \right], \quad (52)$$

where $y_2 = 4.0$ and $y_3 = 1.0$ restricted the perturbation in $1.0 \leq |y| \leq 4.0$, and $H_{pt} = 0.5$. $\lambda = 7.5\pi$ was chosen so that the wavelength of the applied perturbation corresponded to the fastest growing mode of the Parker instability under the present initial conditions (figure 6(a)). A benchmark test was conducted in a simulation domain of $-7.5\pi \leq x \leq 7.5\pi$ and $-15\pi \leq y \leq 15\pi$ with the periodic boundary condition in the x -direction and the free boundary condition in the y -direction. The scale height H_0 was resolved by $20/\pi$ cells (300×600 cells).

Figure 6(b) shows the time evolution of the Fourier amplitude of the initial perturbation ($m = 2$). We found that the most unstable mode grew exponentially until $t = 50$ at a rate expected from the

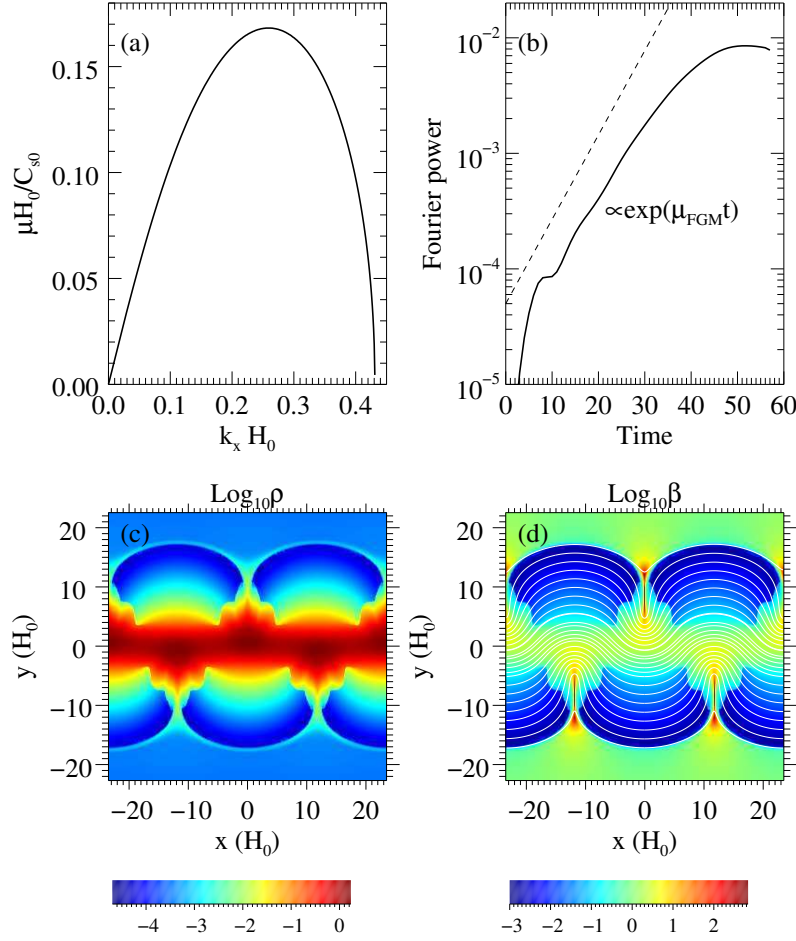


Fig. 6. (a) Linear growth rate of the Parker instability as a function of the wavenumber in the x -direction. (b) Time evolution of the Fourier power of the $m=2$ mode (the fastest growing mode) of B_y by CANS+. The dashed line indicates the linear growth rate from the linear analysis in (a). (c) Mass density and (d) plasma β profiles at $T = 50$ in logarithmic scales. Magnetic field lines are represented by white solid lines in (d).

linear analysis (figure 6(a)).

In the nonlinear stage, magnetic loops were lifted up by the buoyancy force against the magnetic tension force. The plasma inside the loops fell down along the field lines creating high-density regions in the footpoints (figure 6(c)). The loop-top region therefore became rarefied in the nonlinear stage. Usual finite volume methods based on the conservative form of the MHD equations eventually result in disastrous numerical solutions in such a rarefied, low- β plasma, but CANS+ successfully solved its evolution in which the mass density and the plasma β decreased down to $\sim 10^{-5}$ and $\sim 10^{-3}$ (figure 6(c) and 6(d)), respectively, in the late nonlinear stage by virtue of the prescriptions presented in subsection 2.5.

3.2.4 Magnetic reconnection

When magnetic field lines are imposed to form an antiparallel geometry, the magnetic field topology changes through reconnection of the field lines. Because it accompanies the magnetic energy conversion to the plasma kinetic energy, the magnetic reconnection has been studied extensively to understand explosive phenomena, such as flares in the solar corona and pulsar winds, and terrestrial substorms. It is also an important process in dynamo processes in accretion disks. The topology change during reconnection is characterized by bent magnetic field lines and bipolar trans-Alfvénic jets from the reconnecting “x” point, and the resulting plasmoid evolution. It was recently found by performing high-resolution MHD simulations that various MHD shock waves and discontinuities are formed as a result of interactions between the jet and plasmas surrounding the plasmoid (Zenitani and Miyoshi 2011; Zenitani 2015). Here we present the code’s capability of capturing such structures and turbulence associated with the plasmoid evolution. To initiate the reconnection, the resistivity η terms on the right-hand side of equations (3) and (4) were retained.

We examined simulation runs following Zenitani and Miyoshi (2011), in which initial configurations were given as the Harris equilibrium: $B_x = B_0 \tanh(y/\lambda)$, $B_y = B_z = 0$, $\mathbf{V} = 0$, $\rho = \rho_0(1 + \cosh^{-2}(y/\lambda)/\beta_0)$, $p = 0.5B_0^2(\beta_0 + \cosh^{-2}(y/\lambda))$, where λ is the current sheet half-thickness. The resistivity was locally added in the simulation domain around the “x” point as $\eta = \eta_0 + (\eta_1 - \eta_0) \cosh^{-2}(\sqrt{x^2 + y^2}/\lambda)$. Perturbations were initially added to B_x and B_y components through the vector potential of $\delta A_z = 0.06B_0\lambda \exp[-(x^2 + y^2)/4\lambda^2]$. To save computation time, we only solved one quadrant of the reconnection region by applying symmetric conditions at $x = 0$ and $y = 0$. The simulation domain was therefore $0 \leq x \leq 200\lambda$ and $0 \leq y \leq 50\lambda$ with λ being resolved by 30 computational cells (6000×1500 cells). The spacial length, velocity, and time were normalized to λ , $V_{A0} = B_0/\sqrt{\rho_0}$, and λ/V_{A0} with $B_0 = \rho_0 = 1.0$, $\beta_0 = 0.2$ and $\eta_1 = 1/60$. We set $\eta_0 = 0.0$ to highlight the code’s capability.

Figure 7 shows V_x profiles at $t = 250$ characterizing a heart-shaped plasmoid structure downstream of the reconnection region. The plasmoid is formed as a result of interaction between the collimated jet from the reconnection region ($V_x > \sim 1$ in $x < 62$ and $-3 < y < 3$) and the stationary plasma in the current sheet. Vertical slow shock wave fronts in the outer ($x \sim 104$) and postplasmoid ($x \sim 53$) regions, and multiple reflections of shock waves (shock diamonds) in the current sheet ($105 \leq x \leq 127$) were clearly captured by both the MP5 and MUSCL schemes (figure 7(a) and 7(b)) in addition to the various MHD discontinuities and shock waves, as reported previously (Zenitani and Miyoshi 2011).

The plasmoid motion in the x -direction pushes the stationary plasma away from the current sheet in $85 < x < 88$ to $z \sim \pm 2$, making the velocity shear between the swept and surrounding plasmas.

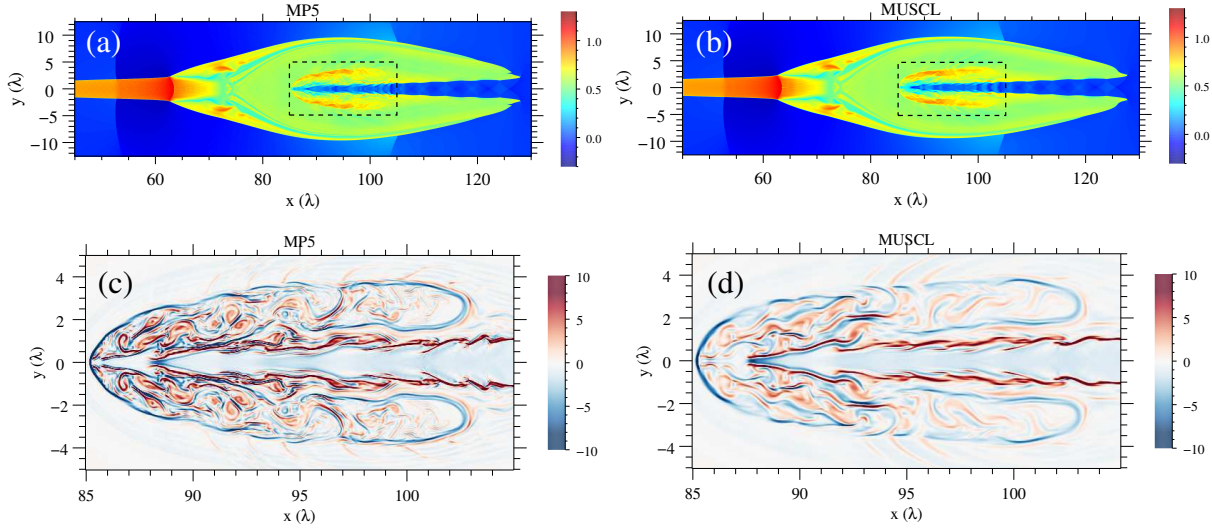


Fig. 7. (a) and (b) Profiles of the x -component of the velocity at $T = 250$ for the MP5 and MUSCL schemes, respectively, characterizing a heart-shaped structure of the plasmoid downstream of the reconnection region. A mirrored image in $y < 0$ is also shown for visual purposes. (c) and (d) Enlarged views of the z -component of the current density ($\nabla \times \mathbf{B}$) in the area surrounded by dashed lines in (a) and (b) for the MP5 and MUSCL schemes, respectively. The color scale is saturated at ± 10 to visually identify fine-scale structures inside and around the jets.

This velocity profile can be a source of turbulence through excitation of the K–H instability (Zenitani and Miyoshi 2011). Figure 7(c) and 7(d) show enlarged views of the z -component of the current density ($\nabla \times \mathbf{B}$) in the area surrounded by dashed lines in figures 7(a) and 7(b). In Figure 7(c), one can see a series of oblique red lines at $90 < x < 100$, $y = \pm 4$. They correspond to small shocks in front of the humps of the K–H waves. Although the large-scale pictures looked similar in the MP5 and MUSCL runs (figure 7(c) and 7(d)), the MP5 scheme resolved both the shocklets and the highly turbulent current vortices much better.

4 Application to Global Simulations of a Black Hole Accretion Disk

In this section, we present global simulations of an accretion disk around a black hole as an application of CANS+. The long-term evolution was characterized by a sharp contact discontinuity between the hot, dilute corona and the cold, dense, rotating disk, compressible magnetic turbulence via the magnetorotational instability (MRI), the resulting mass accretion (advection), and the periodic dynamo process through the Parker instability (Machida et al. 2013). All of these mechanisms were successfully solved by adopting the HLLD approximate Riemann solver, the MP5 reconstruction, and the hyperbolic divergence cleaning method in CANS+.

4.1 Initial torus model

We examined the evolution of an accretion disk initially given as a torus threaded by the toroidal magnetic field embedded in nonrotating, hot and dilute plasma (corona) (Okada et al. 1989; Machida and Matsumoto 2003). General relativistic effects around the black hole are modeled by the pseudo-Newtonian gravitational potential (Paczynsky and Wiita 1980),

$$\phi = -\frac{GM}{R - R_S}, \quad (53)$$

where R is radial distance from the black hole in spherical coordinates, G is the gravitational constant, M is the black hole mass, and R_S is the Schwarzschild radius. Then the gravitational acceleration was obtained by $\mathbf{g} = -\nabla\phi$.

Magnetic field dissipation and the resulting ohmic heating were incorporated by adopting the anomalous resistivity model (Yokoyama and Shibata 1994)

$$\eta = \eta_0 \left[\max \left(\frac{v_d}{v_c} - 1, 0 \right) \right]^2, \quad (54)$$

where $v_d = \mathbf{j}/[\rho(j_0/\rho_0)]$ is the normalized drift speed for the current density and v_c is a critical speed that determined the threshold for activating the anomalous resistivity.

The torus was initially given by setting a density profile (Nishikori et al. 2006) as

$$\rho = \rho_0 \left\{ \frac{\max[\Psi_0 - \phi - L^2/2r^2, 0]}{K\gamma/(\gamma-1) \left(1 + \beta_0^{-1}r^{2(\gamma-1)}/r_0^{2(\gamma-1)}\right)} \right\}^{1/(\gamma-1)}, \quad (55)$$

where r_0 , ρ_0 and β_0 are the values at the center of the torus at which the mass density has a maximum value, $K = p/\rho^\gamma$, and L is the specific angular momentum that is constant inside the torus. Ψ_0 is the potential energy at $r = r_0$ given by

$$\Psi_0 = \phi_0 + \frac{L}{2r_0^2} + \frac{C_{s0}^2}{\gamma-1} \left(1 + \frac{1}{\beta_0}\right), \quad (56)$$

which is constant provided the Alfvén speed for the toroidal magnetic field ($\sqrt{B_\phi^2/\rho}$) inside the torus is a function of rB_ϕ (Okada et al. 1989). The mass density for the corona was given by (Nishikori et al. 2006)

$$\rho_c = 10^{-4}\rho_0 \exp\left(-\frac{\gamma}{C_{sc}^2}(\phi - \phi_0)\right), \quad (57)$$

where $C_{sc} = \sqrt{\gamma P_c/\rho_c}$ is the characteristic sound speed in the corona.

4.2 Numerical setup

The time evolution of the black hole accretion disk was obtained by solving the GLM–MHD equations (eqs. (1) - (5)) in cylindrical coordinates (see subsection 2.6). The spacial length, velocity, and time

were normalized to the initial torus position (r_0), the rotating speed of the torus ($V_0 = L/r_0$), and the rotational period ($t_0 = 2\pi r_0/V_0$), respectively, and we will discuss in units of $r_0 = V_0 = \rho_0 = 1$. In the following numerical experiments, we adopted $\gamma = 5/3$, $\beta_0 = 100$, $R_S = 0.1$, $v_c = 3.6$, and $P_c = 3 \times 10^2 P_0$. The number of computational cells in each direction was $(N_r, N_\phi, N_z) = (256, 64, 264)$. The cell sizes in the r - and z -directions were $\Delta r = 0.01$ in $0 \leq r \leq 0.96$ and $\Delta z = 0.01$ in $-0.44 \leq z \leq 0.44$. Outside these regions, the cell sizes were increased by 5% with respect to the neighboring cell size as $\Delta r_{i+1}/\Delta r_i = \Delta z_{k+1}/\Delta z_k = 1.05$, where i and k are the cell number, and are bounded by a maximum value of 0.1. The cell size in the ϕ -direction was $\Delta\phi = 2\pi/N_\phi$. The computational domain consequently covered $0 \leq r \leq 14.1$, $0 \leq \phi \leq 2\pi$, and $-6.4 \leq z \leq 6.4$.

The periodic boundary condition was applied in the ϕ -direction, whereas the free boundary condition was applied in the z -direction and the outermost region in the r -direction. All physical quantities were absorbed inside the spherical region of $R \leq 0.2$. This was accomplished by damping deviation of a physical quantity, q , from the initial state q_0 with a damping rate a_i as (Machida and Matsumoto 2003)

$$a_i = 0.1 \left[1.0 - \tanh \left(\frac{R - 0.2 + 5\Delta r}{2\Delta r} \right) \right], \quad (58)$$

$$q^{new} = q - a_i(q - q_0). \quad (59)$$

4.3 Results

Using the same initial setup, we compared results from the MP5 and MUSCL schemes. Figure 8 shows the time evolution of the accretion disk solved by the MP5 scheme. Inside the torus threaded by the azimuthal magnetic field, the MRI exponentially grew (figure 8(a), 8(d), and 8(g)) until $t = 20$. The Maxwell stress ($B_r B_\phi$) generated by the MRI (figure 8(e), 8(f), 8(h), and 8(i)) enhanced outward momentum transport, resulting in continuous mass accretion into the black hole (figure 8(b) and 8(c)).

After nonlinear saturation of the MRI, the poloidal component of the magnetic field was created via the Parker instability, allowing escape of magnetic flux to the corona, which in turn caused a reversal of the sign of the azimuthal component inside the disk (Machida et al. 2013) (figure 8(d)–8(f)). This reversal of the toroidal magnetic field occurred periodically during its long-term evolution until $t = 50$ in the simulation run with the MP5 scheme. Figure 9(a) shows a butterfly diagram for the azimuthal component of the magnetic field averaged in the region $0.75 \leq r \leq 1.25$ and $0 \leq \phi \leq 2\pi$. Reversals of the sign of the magnetic field at the disk center occurred after the preceding buoyant motions of the magnetic flux due to the Parker instability. This dynamo process persisted during the simulation run with a periodicity of $t \sim 10$.

When we examined the same problem with the MUSCL scheme, such a dynamo process

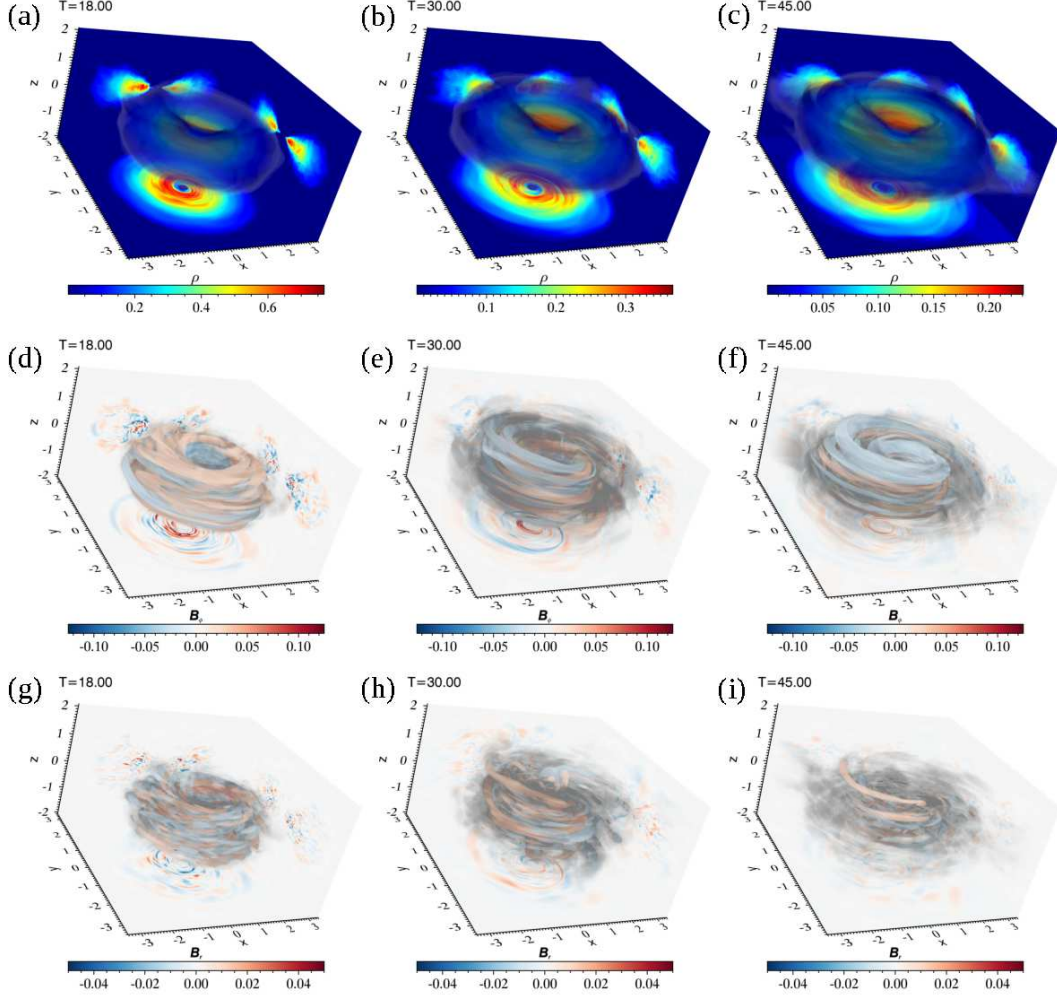


Fig. 8. Time evolution of the accretion disk obtained by the MP5 scheme. From left to right, snapshots at $t = 18.0$ (first column), $t = 30.0$ (second column), and $t = 45.0$ (last column) are shown for the mass density (top row) and ϕ - and r -components of the magnetic field (middle and bottom rows). Profiles at the equatorial and meridian planes passing through the black hole are projected on the x - y , x - z , and y - z planes.

occurred only in the initial phase of the evolution, as shown in figure 9(b). After the initial reversal of the magnetic field sign in the disk center, negative components survived for long periods followed by a faint reversal to positive values at $t \sim 40$. The TVD property of the MUSCL scheme evidently inhibited turbulence and dynamo processes during the long-term evolution. This drawback is also visually recognized in figure 10, in which the ϕ -component of the magnetic field (figure 10(a)–10(c)) suffered from strong numerical damping in time scales of a few tens of rotational periods. It is also of interest that the r -component almost disappeared after long-term evolution (figure 10(d)–10(f)), indicating that activity of the MRI and the resulting angular momentum transport ceased in the final stage of the simulation run.

Figure 11(a) compares the time histories of the mass accretion rate calculated at the inner

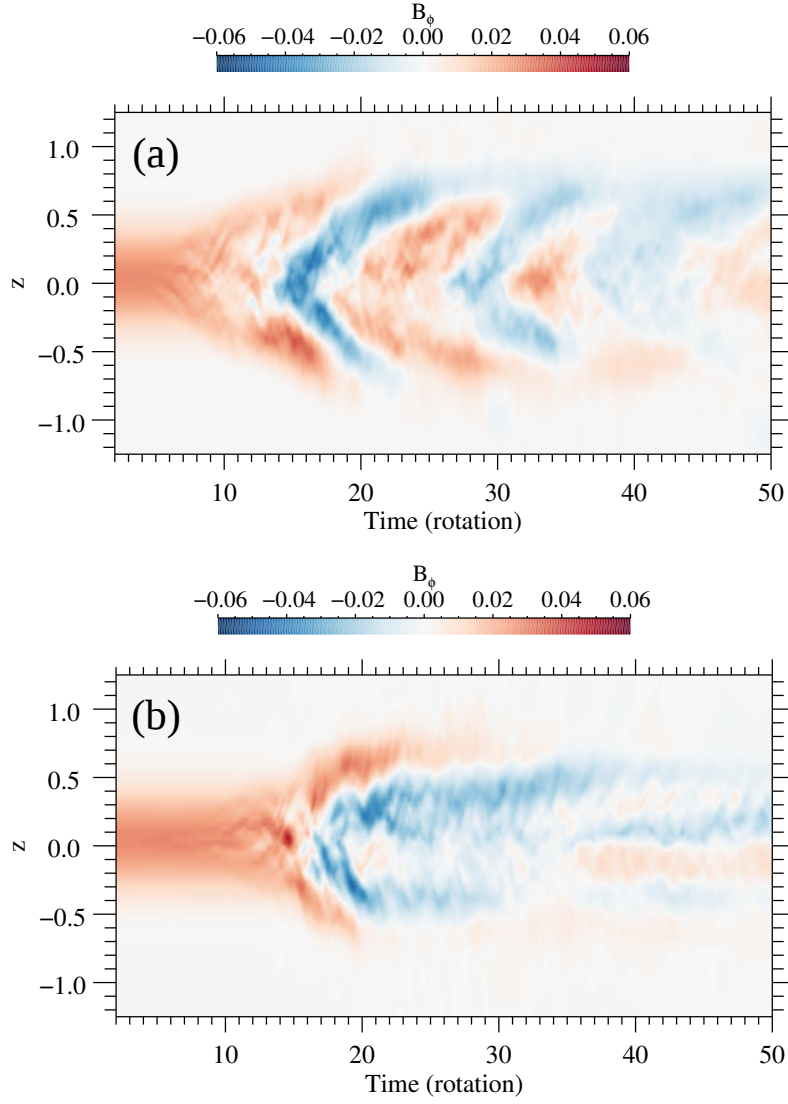


Fig. 9. Butterfly diagram for the azimuthal component of the magnetic field from results by the (a) MP5 and (b) MUSCL schemes.

boundary as (Stone and Pringle 2001)

$$\dot{M} = 2\pi R_0^2 \int_0^\pi \rho v_R \sin(\theta) d\theta, \quad (60)$$

where $R_0 = 0.2$ and θ are the radius at the inner boundary and the elevation angle in spherical coordinates, respectively. The mass accretion rate peaked at $t \sim 20$ and gradually decreased and maintained a certain level until $t = 50$ in the run with the MP5 scheme (red line). In contrast, the mass accretion decayed and completely ceased at $t = 40$ following the peak in rate at $t \sim 20$ with the MUSCL scheme (blue line).

The mass accretion stopped in the MUSCL run because the amplitude of the MRI became very weak in the late stage of the run. The activity can be quantified by the so-called α -parameter (Shakura and Sunyaev 1973)

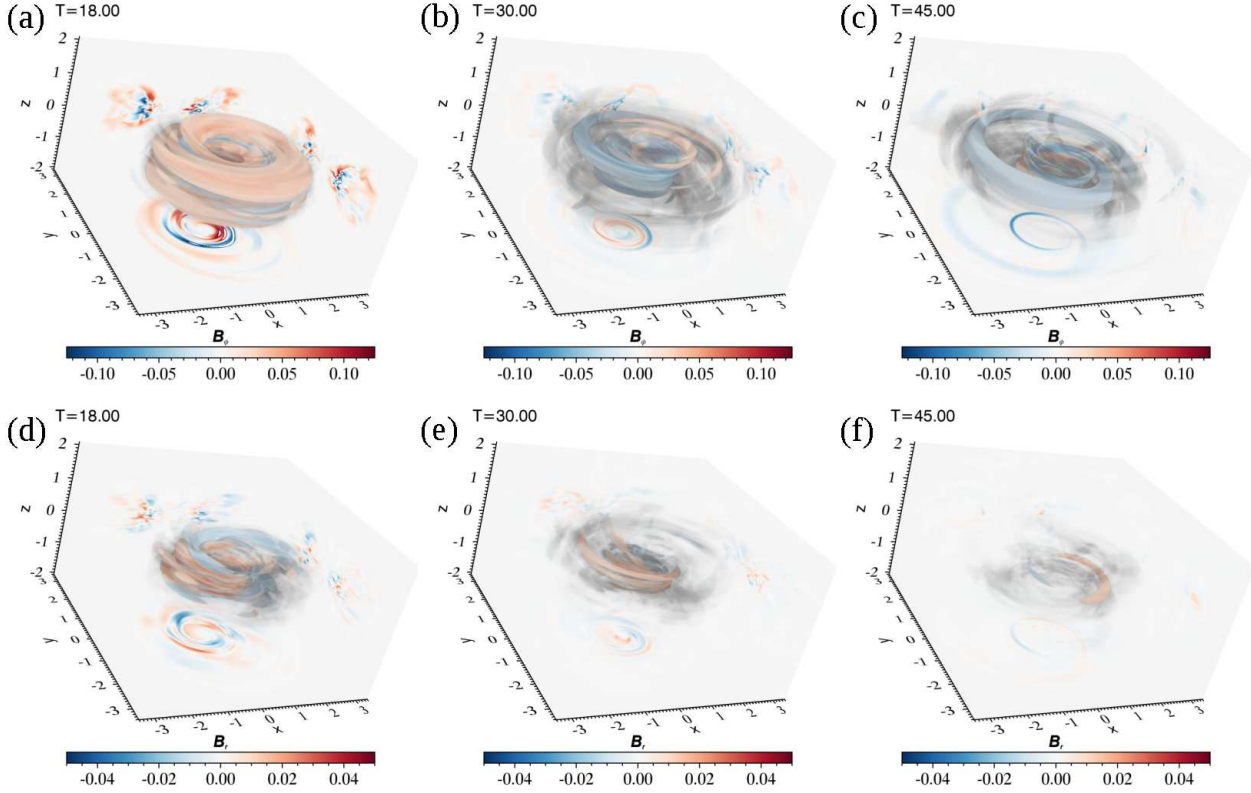


Fig. 10. Time evolution of the accretion disk obtained by the MUSCL scheme. The format is the same as figure 8 but only for the azimuthal ((a)–(c)) and the radial ((d)–(f)) components of the magnetic field.

$$\alpha = - \left\langle \frac{B_r B_\phi}{P} \right\rangle, \quad (61)$$

where $\langle \rangle$ stands for the volume-weighted average of the quantity in cylindrical coordinates. Figure 11(b) compares time histories of the α -parameter averaged in a region, $0.2 \leq r \leq 0.5$, $0 \leq \phi \leq 2\pi$, and $-0.25\pi \leq \arcsin(z/\sqrt{r^2 + z^2}) \leq +0.25\pi$. The range of the α -parameter was 0.02–0.04 with a peak value of $\alpha = 0.08$ during $t = 20$ –50 in the MP5 run (red line). The sustained activity enabled continuous mass accretion in figure 11(a). In contrast, for the MUSCL scheme run (blue line), the α -parameter was systematically as low as $\alpha \leq 0.01$ and eventually it was almost zero in the later stages of the run ($t \geq 40$), resulting in the suspension of the mass accretion.

5 Summary and Discussion

We have developed CANS+, a high-resolution, numerically robust MHD simulation code by employing the HLLD approximate Riemann solver, the MP5 reconstruction method, and the hyperbolic divergence cleaning method. We performed a number of benchmark tests to show the code’s capabil-

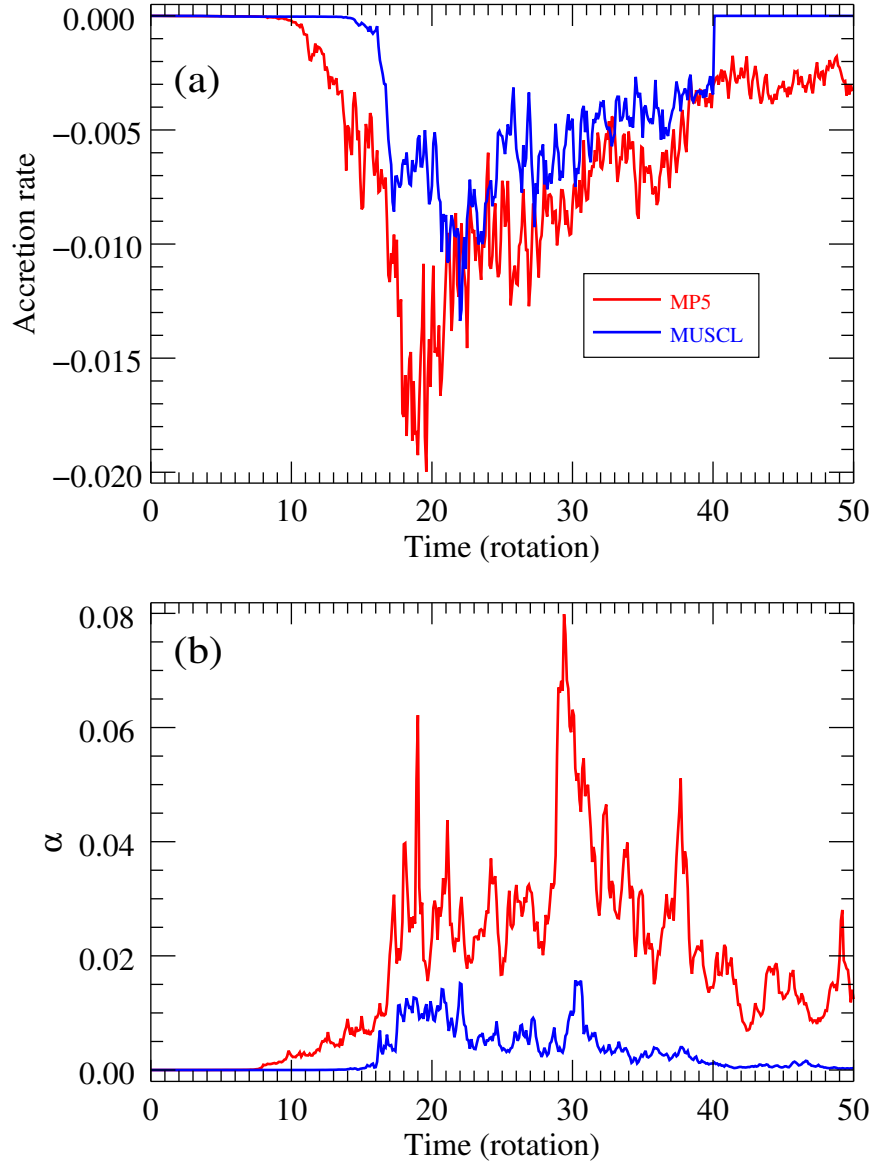


Fig. 11. Time evolution of (a) the mass accretion rate (eq. 60) and (b) α -parameter (eq. 61) obtained by the MP5 (red line) and MUSCL (blue line) schemes.

ity for solving discontinuities, shock waves, and turbulence all of which are essentially important in astrophysical situations.

In 1D benchmark tests that included linear Alfvén wave propagation and shock tube problems, the adoption of a spatial fifth-order scheme gave superior results compared with a second-order scheme, even when the additional computational costs arising from the higher-order reconstruction were considered: The computation time increased by a few times compared with the second-order scheme, but for the same grid resolution the numerical errors from the fifth-order scheme were smaller by orders of magnitude. In other words, to obtain solutions with the same accuracy, the fifth-order scheme required smaller numerical costs by orders of magnitude than the second-order scheme. This advantage is more prominent in multidimensional problems.

In 2D tests of the K–H turbulence, the Orszag–Tang vortex problem, and the magnetic reconnection, it was shown that CANS+ enables solving discontinuities, shock waves, and turbulence with high accuracy and stability simultaneously. The test problem of the Parker instability also showed a high capability for solving very low- β ($\sim 10^{-3}$) plasma in which the numerical divergence errors of the magnetic field were maintained within reasonably low levels.

As an application of CANS+, we presented global simulations of an accretion disk around a black hole. With a given initial setup and grid resolution, CANS+ was capable of following the long-term evolution of the accretion disk in which the MRI and the resulting mass accretion into the black hole were sustained for 50 rotational periods. While the long-term evolution characterized by compressible MHD turbulence clearly benefited from adoption of the fifth-order scheme, it quickly decayed in the results from the second-order scheme because of the strong numerical damping effects of the TVD property.

Lastly, we address the caveat of using fifth-order numerical schemes. The characteristic variables used for the reconstruction step showed the best performance with nonoscillatory results in the 1D shock tube problem. With other parameters, such as primitive variables, the updated conservative variables profiles were subject to numerical oscillations around discontinuities even if the MP5 reconstruction gave nonoscillatory profiles at cell surfaces. Thus, the reconstruction step not only required high computational costs because of the variable conversion, but also introduced difficulty in analytically obtaining the eigenvectors and the corresponding eigenvalues of the system. This can be problematic when extending the present MHD to, for example, the special relativistic MHD equations, in which the second-order TVD schemes have been adopted (Matsumoto et al. 2011; Takahashi and Ohsuga 2013). The search for variables that are universally applicable to high-order reconstruction in various systems of equations remains a task for further applications of CANS+.

Acknowledgments

CANS+ was based on the code originally developed by T. Ogawa at Chiba University. The numerical setup for magnetic reconnection was developed by N. Iwamoto, A. Kawamura, J. Sakamoto, and T. Shibayama during the simulation summer school held at Chiba University in 2014. The present simulations used computational resources provided by the Information Technology Center, the University of Tokyo, Research Institute for Information Technology, Kyushu University, and the RIKEN Advanced Institute for Computational Science through the HPCI System Research project (Project ID: hp120193, hp120287, hp130027, hp140213, hp150227), and Cray XC30 at Center for Computational Astrophysics, National Astronomical Observatory of Japan. This work was supported in part by MEXT SPIRE, MEXT as Priority Issue on Post-K computer (Elucidation of the Fundamental Laws and Evolution of the Universe), and JICFuS.

References

- N. Asai, N. Fukuda, and R. Matsumoto. Magnetohydrodynamic simulations of the formation of cold fronts in clusters of galaxies including heat conduction. *Astrophys. J.*, 606:L105–L108, 2004.
- J. Brackbill and D. Barnes. The Effect of Nonzero $\nabla \cdot \mathbf{B}$ on the Numerical Solution of the Magnetohydrodynamic Equations. *J. Comput. Phys.*, 430:426–430, 1980.
- M. Brio and C. Wu. An upwind differencing scheme for the equations of ideal magnetohydrodynamics. *J. Comput. Phys.*, 75(2):400–422, 1988.
- P. Colella and P. R. Woodward. The Piecewise Parabolic Method (PPM) for gas-dynamical simulations. *J. Comput. Phys.*, 54(1):174–201, 1984.
- A. Dedner, F. Kemm, D. Kröner, C.-D. Munz, T. Schnitzer, and M. Wesenberg. Hyperbolic Divergence Cleaning for the MHD Equations. *J. Comput. Phys.*, 175(2):645–673, 2002.
- C. R. Evans and J. F. Hawley. Simulation of magnetohydrodynamic flows - A constrained transport method. *Astrophys. J.*, 332(2):659, 1988.
- T. A. Gardiner and J. M. Stone. An unsplit Godunov method for ideal MHD via constrained transport. *J. Comput. Phys.*, 205(2):509–539, 2005.
- S. Gottlieb and C.-W. Shu. Total variation diminishing Runge-Kutta schemes. *Math. Comput. Am. Math. Soc.*, 67(221):73–85, 1998.
- H. Hanayama, K. Takahashi, K. Kotake, M. Oguri, K. Ichiki, and H. Ohno. Biermann Mechanism in Primordial Supernova Remnant and Seed Magnetic Fields. *Astrophys. J.*, 633(2):941–945, 2005.
- A. Harten, P. D. Lax, and B. van Leer. On Upstream Differencing and Godunov-Type Schemes for Hyperbolic Conservation Laws. *SIAM Rev.*, 25(1):35–61, 1983.
- A. Harten, B. Engquist, S. Osher, and S. R. Chakravarthy. Uniformly high order accurate essentially non-oscillatory schemes, III. *J. Comput. Phys.*, 71(2):231–303, 1987.
- J. F. Hawley and J. M. Stone. MOCCT: A numerical technique for astrophysical MHD. *Comput. Phys. Commun.*, 89(1-3):127–148, 1995.

- H. Isobe, T. Miyagoshi, K. Shibata, and T. Yokoyama. Filamentary structure on the Sun from the magnetic RayleighTaylor instability. *Nature*, 434(7032):478–481, 2005.
- A. G. Kritsuk, Å. Nordlund, D. Collins, P. Padoan, M. L. Norman, T. Abel, R. Banerjee, C. Federrath, M. Flock, D. Lee, P. Shing Li, W.-C. Müller, R. Teyssier, S. D. Ustyugov, C. Vogel, and H. Xu. Comparing Numerical Methods for Isothermal Magnetized Supersonic Turbulence. *Astrophys. J.*, 737(1):13, 2011.
- T. Kudoh, R. Matsumoto, and K. Shibata. Magnetically Driven Jets from Accretion Disks. III. 2.5dimensional Nonsteady Simulations for Thick Disk Case. *Astrophys. J.*, 521(2):934–934, 1999.
- D. Lee. A solution accurate, efficient and stable unsplit staggered mesh scheme for three dimensional magnetohydrodynamics. *J. Comput. Phys.*, 243:269–292, 2013.
- D. Lee and A. E. Deane. An unsplit staggered mesh scheme for multidimensional magnetohydrodynamics. *J. Comput. Phys.*, 228(4):952–975, 2009.
- S. Li. An HLLC Riemann solver for magneto-hydrodynamics. *J. Comput. Phys.*, 203(1):344–357, 2005.
- P. Londrillo and L. Del Zanna. On the divergence-free condition in Godunov-type schemes for ideal magneto-hydrodynamics: The upwind constrained transport method. *J. Comput. Phys.*, 195:17–48, 2004.
- M. Machida and R. Matsumoto. Global Three-dimensional Magnetohydrodynamic Simulations of Black Hole Accretion Disks: X-Ray Flares in the Plunging Region. *Astrophys. J.*, 585(1):429–442, 2003.
- M. Machida, K. E. Nakamura, T. Kudoh, T. Akahori, Y. Sofue, and R. Matsumoto. Dynamo Activities Driven By Magnetorotational Instability and the Parker Instability in Galactic Gaseous Disks. *Astrophys. J.*, 764(1): 81, 2013.
- J. Matsumoto, Y. Masada, E. Asano, and K. Shibata. Special relativistic magnetohydrodynamic simulation of a two-component outflow powered by magnetic explosion on compact stars. *Astrophys. J.*, 733(1):18, 2011.
- R. Matsumoto, T. Horiuchi, K. Shibata, and T. Hanawa. Parker Instability in Nonuniform Gravitational Fields - Part Two - Nonlinear Time Evolution. *Publ. Astron. Soc. Japan*, 40(2):171, 1988.
- Y. Matsumoto and M. Hoshino. Onset of turbulence induced by a Kelvin-Helmholtz vortex. *Geophys. Res. Lett.*, 31(2):L02807, 2004.
- Y. Matsumoto and K. Seki. Formation of a broad plasma turbulent layer by forward and inverse energy cascades of the KelvinHelmholtz instability. *J. Geophys. Res.*, 115(A10):A10231, 2010.
- A. Mignone, G. Bodo, S. Massaglia, T. Matsakos, O. Tesileanu, C. Zanni, and A. Ferrari. PLUTO: A Numerical Code for Computational Astrophysics. *Astrophys. J. Suppl. Ser.*, 170(1):228–242, 2007.
- A. Mignone, P. Tzeferacos, and G. Bodo. High-order conservative finite difference GLM-MHD schemes for cell-centered MHD. *J. Comput. Phys.*, 229(17):5896–5920, 2010.
- T. Minoshima, S. Hirose, and T. Sano. Dependence of the saturation level of magnetorotational instability on gas pressure and magnetic Prandtl number. *Astrophys. J.*, 808(1):54, 2015.

- T. Miyoshi and K. Kusano. A multi-state HLL approximate Riemann solver for ideal magnetohydrodynamics. *J. Comput. Phys.*, 208(1):315–344, 2005.
- T. Miyoshi and K. Kusano. A Comparative Study of Divergence-Cleaning Techniques for Multi-Dimensional MHD Schemes. *Plasma Fusion Res.*, 6(1 SPECIAL ISSUE):2401124–2401124, 2011.
- H. Nishikori, M. Machida, and R. Matsumoto. Global Three-dimensional Magnetohydrodynamic Simulations of Galactic Gaseous Disks. I. Amplification of Mean Magnetic Fields in an Axisymmetric Gravitational Potential. *Astrophys. J.*, 641(2):862–877, 2006.
- R. Okada, J. Fukue, and R. Matsumoto. A model of Astrophysical Tori with magnetic fields. *Publ. Astron. Soc. Japan*, 41:133–140, 1989.
- S. A. Orszag and C.-M. Tang. Small-scale structure of two-dimensional magnetohydrodynamic turbulence. *J. Fluid Mech.*, 90(01):129, 1979.
- B. Paczyński and P. J. Wiita. Thick accretion disks and supercritical luminosities. *Astron. Astrophys.*, 88: 23–31, 1980.
- E. N. Parker. The Dynamical State of the Interstellar Gas and Field. *Astrophys. J.*, 145:811, 1966.
- K. G. Powell, P. L. Roe, T. J. Linde, T. I. Gombosi, and D. L. De Zeeuw. A Solution-Adaptive Upwind Scheme for Ideal Magnetohydrodynamics. *J. Comput. Phys.*, 154(2):284–309, 1999.
- P. Roe. Approximate Riemann solvers, parameter vectors, and difference schemes. *J. Comput. Phys.*, 43(2): 357–372, 1981.
- E. L. Rubin and S. Z. Burstein. Difference methods for the inviscid and viscous equations of a compressible gas. *J. Comput. Phys.*, 2(2):178–196, 1967.
- D. Ryu and T. W. Jones. Numerical magnetohydrodynamics in astrophysics: Algorithm and tests for one-dimensional flow. *Astrophys. J.*, 442:228, 1995.
- N. I. Shakura and R. A. Sunyaev. Black holes in binary systems. Observational appearance. *Astron. Astrophys.*, 24:337–355, 1973.
- K. Shibata. Nonlinear MHD wave propagation in the solar chromosphere. I The case of a uniform vertical magnetic field. *Publ. Astron. Soc. Japan*, 35:263–284, 1983.
- J. M. Stone and J. E. Pringle. Magnetohydrodynamical non-radiative accretion flows in two dimensions. *Mon. Not. R. Astron. Soc.*, 322(3):461–472, 2001.
- J. M. Stone, J. F. Hawley, C. R. Evans, and M. L. Norman. A test suite for magnetohydrodynamical simulations. *Astrophys. J.*, 388:415, 1992.
- J. M. Stone, T. A. Gardiner, P. Teuben, J. F. Hawley, and J. B. Simon. Athena: A New Code for Astrophysical MHD. *Astrophys. J. Suppl. Ser.*, 178(1):137–177, 2008.
- A. Suresh and H. Huynh. Accurate Monotonicity-Preserving Schemes with Runge–Kutta Time Stepping. *J. Comput. Phys.*, 136(1):83–99, 1997.

- H. R. Takahashi and K. Ohsuga. A numerical treatment of anisotropic radiation fields coupled with relativistic resistive magnetofluids. *Astrophys. J.*, 772(2):127, 2013.
- C. Tao, R. Kataoka, H. Fukunishi, Y. Takahashi, and T. Yokoyama. Magnetic field variations in the Jovian magnetotail induced by solar wind dynamic pressure enhancements. *J. Geophys. Res.*, 110(A11):A11208, 2005.
- S. Toriumi and T. Yokoyama. Numerical Experiments on the Two-Step Emergence of Twisted Magnetic Flux Tubes in the Sun. *Astrophys. J.*, 735(2):126, 2011.
- G. Toth. The $\nabla \cdot \mathbf{B} = 0$ Constraint in Shock-Capturing Magnetohydrodynamics Codes. *J. Comput. Phys.*, 161: 605–652, 2000.
- K. Tsubouchi. Alfvén wave evolution within corotating interaction regions associated with the formation of magnetic holes/decreases. *J. Geophys. Res.*, 114(A2), 2009.
- B. van Leer. Towards the ultimate conservative difference scheme. V. A second-order sequel to Godunov’s method. *J. Comput. Phys.*, 32(1):101–136, 1979.
- T. Yabe, F. Xiao, and T. Utsumi. The constrained interpolation profile method for multiphase analysis. *J. Comput. Phys.*, 169(2):556–593, 2001.
- T. Yokoyama and K. Shibata. What is the condition for fast magnetic reconnection? *Astrophys. J.*, 436:L197, 1994.
- S. Zenitani. Magnetohydrodynamic structure of a plasmoid in fast reconnection in low-beta plasmas: Shock-shock interactions. *Phys. Plasmas*, 22(3):032114, 2015.
- S. Zenitani and T. Miyoshi. Magnetohydrodynamic structure of a plasmoid in fast reconnection in low-beta plasmas. *Phys. Plasmas*, 18(2):022105, 2011.